Title

Sensitivity of geophysical techniques for monitoring secondary CO2 storage plumes

Authors
Gasperikova, Erika
Appriou, Delphine
Bonneville, Alain
et al.

Publication Date
2022-02-01

DOI
10.1016/j.ijggc.2022.103585

Sensitivity of geophysical techniques for monitoring secondary CO_2 storage plumes

Erika Gasperikova[1], Delphine Appriou[2], Alain Bonneville[2,5], Zongcai Feng[3], Lianjie Huang[3], Kai Gao[3], Xianjin Yang[4], Thomas Daley[1]

[1] Lawrence Berkeley National Laboratory, 1 Cyclotron Road, Berkeley, CA 94720

[2] Pacific Northwest National Laboratory, 902 Battelle Boulevard, Richland, WA 99354

[3] Los Alamos National Laboratory, MS D452, Los Alamos, NM 87545

[4] Lawrence Livermore National Laboratory, 7000 East Avenue, Livermore, CA 94551

[5] College of Earth, Ocean, and Atmospheric Sciences, Oregon State University, Corvallis, OR 97331

Corresponding author: Erika Gasperikova, Lawrence Berkeley National Laboratory, One Cyclotron Road, MS: 74R316C, Berkeley, CA 94720; egasperikova@lbl.gov; 510-486-4930

Conflict of interest: None

Keywords: geophysical monitoring, secondary CO_2 storage plume, seismic, gravity, electromagnetic, sensitivity, post-injection phase

ABSTRACT

For geologic carbon storage, the ability to detect secondary CO_2 plumes—defined as those CO_2 plumes accumulating outside the intended storage reservoir—is fundamental to preventing unexpected CO_2 migration into groundwater resources and for risk and liability management. Understanding the sensitivity of various geophysical methods to secondary plumes is crucial for designing cost-effective monitoring schemes. We use several modeling scenarios to demonstrate the process of assessing sensitivities and detection thresholds of three primary geophysical techniques—surface seismic, borehole-to-surface electromagnetic (EM), and surface and borehole gravity—for early detection of secondary CO_2 plumes in the post-injection phase. While seismic reflection methods are often considered in monitoring strategies to track the evolution of CO_2 plumes, they are also the most expensive. Due to cost considerations, especially for long-term post-injection monitoring, other techniques complement seismic monitoring when designing an adaptive monitoring network. Borehole-to-surface EM or surface gravity surveys are feasible for time-lapse monitoring of deep secondary CO_2 plumes. These surveys could be carried at intervals defined by site-specific conditions. If time-lapse EM and/or gravity surveys detect any signal responses beyond the expected change, it would trigger a need for the higher resolution seismic survey.

1. Introduction

Geologic carbon storage (GCS) is recognized as a viable solution to help achieve carbon neutrality by storing CO_2 in deep geologic formations (Baker et al., 2020; IEA, 2021). Monitoring of subsurface CO_2 plumes is an indispensable component of GCS to account for CO_2 mass in the storage formation, meet regulatory requirements, and assure the public of the containment of CO_2 in the storage reservoir. Despite the successful implementation of multiple CO_2 storage pilot and commercial-scale projects worldwide (Global CCS Institute, 2020), concerns remain about the potential migration of CO_2 out of the targeted storage formations and the ability of monitoring technologies to detect the development of secondary CO_2 accumulations at early stages. Secondary plumes are defined in this study as subsurface accumulations of CO_2 outside of the intended injection/storage reservoir but still within a larger storage complex. The storage complex includes formations above the targeted injection zones with regulatory approval to trap and store migrating CO_2. Previous studies often used leakage and secondary accumulations interchangeably (Pruess, 2008).

1.1 Reservoir monitoring: a mature and proven suite of technologies

A broad range of technologies have been developed, tested, or fully deployed in the field to establish monitoring baselines as part of the site characterization activities and to track changes in subsurface properties during the CO_2 injection phase (Figure 1, left and center panels). These applications include various storage conditions with large or small injection volumes, deep or shallow reservoirs, and offshore or onshore settings (Jenkins et al., 2015). Common monitoring methods include seismic, microseismic, gravity, electrical/electromagnetic, downhole temperature and pressure, well logging, InSAR, fluid sampling, tracer tests, aquifer geochemistry, soil CO_2 concentration, and others (Hovorka et al., 2011; Jenkins et al., 2015; Harbert et al., 2016; Vermeul et al., 2016; Hannis et al., 2017; Daley and Harbert, 2019; Chadwick et al., 2019; Jenkins, 2020). These monitoring technologies can directly, indirectly, and in a complementary manner detect and image CO_2 plumes and fluid pressure changes in the deep subsurface with the ultimate goal of demonstrating that injected CO_2 is effectively and safely contained within the storage complex during the operation phase. Only seismic methods have been deployed at every large-scale GCS project for pre-injection baseline study and time-lapse monitoring during the injection because of their deep penetration depth and high spatial resolution (Jenkins et al., 2015; Ajo-Franklin et al., 2013; Zhang et al., 2013; Roach et al. 2015; Furre et al., 2017).

Monitoring tools evaluated in research GCS projects could become mature tools by the time the first large-scale GCS storage sites enter the post-injection phase. Examples of those include electrical resistivity tomography (ERT), electromagnetic (EM) methods (Girard et al., 2011; Carrigan et al., 2013; Schmidt-Hattenberger et al., 2016; Park et al., 2017; Caesary et al., 2020), gravity monitoring methods (Nooner et al., 2007; Alnes et al., 2008; Alnes et al., 2011; Dodds et al., 2013; Bonneville et al., 2021), and vertical seismic profiling (Hovorka et al., 2011; Coueslan et al., 2013; Daley et al., 2015; Gotz et al., 2014; Bauer et al., 2019; White, 2019; Popik et al., 2020). The diversity and availability of various monitoring tools highlight the importance of adopting a flexible approach during monitoring design that should be adapted as technology improves.

1.2 Post-injection period: a monitoring approach focused on the early detection of secondary CO_2 plumes

Following cessation of CO_2 injection, monitoring activities will continue for a post-injection timeframe established by the regulator (Figure 1, right panel). Dilmore et al. (2021) demonstrated that the risk of unintended CO_2 migration from the storage reservoir rapidly decreases after the injection stops. This decrease justifies a change in the frequency, spatial coverage, and spatial resolution for long-term post-injection monitoring. A monitoring plan should identify technologies that are sensitive enough to detect the emergence of any secondary CO_2 plume before corrective actions (i.e., mitigation actions) are needed.

This study is therefore motivated by the need to understand the limits and expectations of three primary geophysical monitoring methods: seismic, EM, and gravity, which could be implemented for detection of secondary CO_2 accumulations, and ultimately to understand the requirements to design an efficient monitoring strategy for long-term post-injection monitoring at a terrestrial GCS site.

The sensitivity assessment of seismic and EM methods is based on several model scenarios that cover the spectrum from simple synthetic CO_2 models to complex models based on multi-phase flow simulations initially established for the Kimberlina storage complex. Appriou et al. (2020) evaluated the performance of the gravity method on the Kimberlina-2 model. They demonstrated that the gravity response caused by the presence of a secondary CO_2 plume modeled with multi-phase flow simulations could be approached with a simple conceptual model. Building on that finding, we carried out the sensitivity assessment of gravity using simple conceptual models. We selected models with the smallest size or geophysical property changes to exercise the lowest detection limits under the most favorable conditions (e.g., no data noise or limit on data acquisition configurations). We contrasted that with results simulated considering field conditions at a complex GCS site that provide a more realistic sensitivity assessment. These models would be the end members of possible scenarios. A typical GCS site would fall somewhere in the middle.

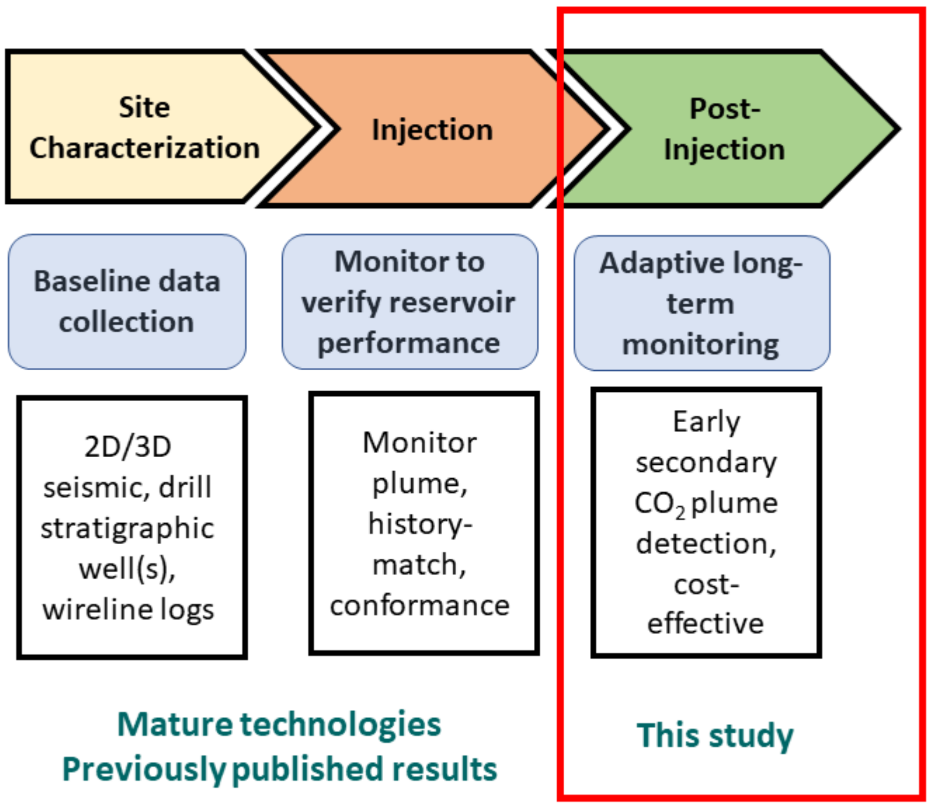

Figure 1. Monitoring at a GCS site and objectives of this study.

1.3 Previous sensitivity studies

Wang et al. (2018) investigated a relationship between seismic survey parameters and sensitivity of 2D surface seismic methods to detect a small CO_2 plume at a depth of 1000 m. Their work illustrated that a 60% increase in shot spacing produced a 30% increase in the maximum of the normalized root-mean-square (nRMS) difference in amplitude caused by the presence of CO_2.

These nRMS difference values, which are a measure of detectability, also increased with a higher source frequency. The measure of nRMS is a standard calculation for qualitative interpretation of seismic monitoring data, which does not require supplementary data on rock properties or a rock physics model of seismic response (Kragh and Christie, 2002). The authors demonstrated that the detection threshold is inversely proportional to the data signal-to-noise ratio (SNR) in the same study. The higher the SNR, the smaller the nRMS that can be used for CO_2 plume detection. A simulation study of CO_2 migration into shallow aquifers by Yang et al. (2019) concluded that a CO_2 mass as small as 350 tonnes could be detected using a detection threshold of 20% nRMS difference in noise-free time-lapse 2D seismic data. In the same study, when sparser survey geometry, a lower source frequency, and a detection threshold of 10% nRMS difference in noise-free data were used, 3D surface seismic data could detect a CO_2 plume of 20,000 tonnes or larger.

Thanks to a peak in commercial applications of marine controlled-source electromagnetics (CSEM) in the first decade of this century, both EM instrumentation and data processing significantly improved and made EM technologies suitable for time-lapse monitoring. Gasperikova and Commer (2019 and references therein) discussed the advantages and limitations of these techniques for CO_2 plume monitoring. Yang et al. (2018a) and Yang et al. (2019) evaluated the detection capabilities of ERT and magnetotellurics (MT) for CO_2 that migrated into shallow aquifers. Using detection thresholds of 10% and 20% change in apparent resistivity for ERT and MT, respectively, the study indicated that both techniques could detect a CO_2 plume of 20,000 tonnes or larger at depths of less than 600 m.

The performance of gravity monitoring solely relies on the mass balance changes over time related to fluid migration in the subsurface. Numerical studies demonstrated that time-lapse surface gravity could be successfully applied as a monitoring tool for GCS (Gasperikova and Hoversten, 2008; Krahenbuhl et al., 2015; Jacob et al., 2016; Appriou et al., 2020; Goto et al., 2020). Borehole gravity surveys applied to GCS or other reservoirs have been numerically assessed (Sherlock et al., 2006; Gasperikova and Hoversten, 2008; Krahenbuhl and Li, 2012; Krahenbuhl et al., 2015; Lofts et al., 2019), but only a limited number of field tests have been undertaken (Dodds et al., 2013; Bonneville et al., 2021). While the advantages of using gravity monitoring for reservoir surveillance have been well established in the literature, efforts to quantitatively constrain the feasibility of the method to detect secondary plumes remain limited (Appriou et al., 2020; Wilkinson et al., 2017).

In this paper, for each of the three primary geophysical monitoring methods (Sections 2-4), we describe the models, the approach, and the results for sensitivity study, including examples of both detectable and undetectable plumes. Section 5 demonstrates how the information from previous sections could be used for monitoring design evaluation when multiple techniques are considered. Finally, we summarize the main findings in the Conclusions.

2. Seismic monitoring

2.1 A synthetic CO_2 plume model

A conceptual model used for this study assumes that CO_2 moves out from the storage reservoir, accumulates in a secondary trap above the storage horizon, and forms a cone-shaped plume. This assumption is reasonable since CO_2 that migrates upward is subject to buoyancy forces and capillary trapping. As the thickness of the secondary trap layer becomes smaller, the difference between the cone-shaped and a cylindrical- or a prism-shaped plume is minimal, and these shapes could be used as a first approximation as was done in gravity monitoring in Section 4. The size of the region containing CO_2 must be sufficient to generate an interpretable signal at the surface. Using a realistic geological model of the subsurface, we made calculations to assess the seismic response of 1,000 tonnes of CO_2 accumulation at depths from 500 to 2000 m. A hydrostatic pore pressure gradient and lithostatic pressure increasing with a gradient of 22.6 kPa/m were assumed, and a geothermal temperature gradient of 30°C/km was used. The density of the CO_2 was obtained using the NIST Mixture Property Database (1992). Table 1 provides the calculated properties for selected depths.

Depth (m)	**T (˚C)**	**P (MPa)**	**CO_2 density (kg/m^3)**	**Phase**
500	30	4.9	120.24	Gas
800	39	7.8	270.35	Supercritical
1000	45	9.8	466.76	Supercritical
1300	54	12.7	570.34	Supercritical
2000	75	19.6	617.11	Supercritical

Table 1. Depths, temperatures, pressure, and CO_2 density used in the calculations.

The secondary trap was a brine-saturated unconsolidated sand layer with a thickness varying from 5 to 100 m, P-wave velocity of 3050 m/s, and density of 2285 kg/m^3. The width of the CO_2 plume is based on the size of the first Fresnel zone, with 2530 m/s P-velocity and 2260 kg/m^3 density. The Fresnel zone defines a lateral dimension of seismic resolution—the area where seismic waves interfere with each other constructively, and it is a function of frequency and seismic velocity. The

P-wave velocity of the shale is 2700 m/s with its density of 2160 kg/m^3. The seismic wave center frequency is 30 Hz. For these conditions, the first Fresnel zone diameter is approximately 320 m. Calculations were carried out for plume widths of 0.5-2.0 Fresnel zones. Full 2D elastic seismic simulations were carried out with and without noise, followed by the production of zero-offset stacked sections and Kirchhoff time migration. The data processing and migration mimicked the steps of conventional field data processing and interpretation.

Sensitivity studies have been conducted to assess the influence of accumulation thickness, CO_2 saturation, and the presence of accumulations at multiple depths. This model also includes the change from supercritical to gas phase, as the CO_2 rises above the 800-m depth when the density decreases and the compressibility increases, which significantly improves seismic detection limits. Based on these parameters, it is possible to calculate the radius of the cone-shaped accumulation. Figure 2 shows plots of radius as a function of depth for a 1,000-tonne accumulation with a range of thicknesses and CO_2 saturations. As expected, when the accumulation moves toward the surface, it becomes significantly larger owing to the associated decrease in density. For the same mass, and a given depth, the plume size is inversely proportional to CO_2 saturation. Note that the volume of a CO_2 plume at 800 m depth is only twice the volume of the plume at 1300 m depth. However, the volume of the same plume at 100 m would be 30 times larger than that at 1300 m depth (caused by the CO_2 change from the supercritical to the gas phase). This observation poses a challenge: Can one design a monitoring array that detects secondary CO_2 plumes before they reach groundwater formations for a cost that is less than possible mitigation costs?

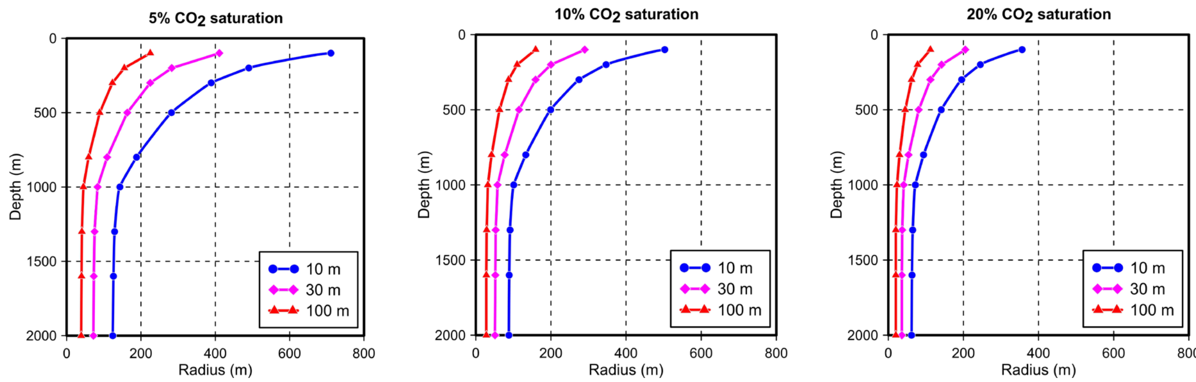

(a) (b) (c)

Figure 2. Size of 1,000 tonne accumulations as a function of depth below the surface for CO_2 saturation of (a) 5%, (b) 10%, and (c) 20%. The radii of the CO_2 plume in 10-, 30-, and 100-m-thick layers are shown in blue, magenta, and red, respectively.

At 2000 m depth, the 5 m thick sand layer model produces no discernable reflection since the layer thickness is on the order of 5% of the seismic wavelength. The 10 m thick sand layer model generated a reflection, but none was observed at the location of the CO_2 plume. The CO_2 plume in a 30 m thick layer can be imaged; the reflections are generated at the brine- and CO_2-saturated sand interface. There is a sufficient thickness of brine-saturated sand beneath the CO_2 wedge to generate a reflection. For these models, the plume width is less than a Fresnel zone, and the layer thickness is similar to or less than the layer tuning thickness. Even though the CO_2 plume is detected, interpretation of the reflection for fluid properties would be difficult because of geometric effects. A plume large enough to prevent contamination of reflections by geometrical effects has a width of about 480 m in 100 m thick sand.

The type and magnitude of noise present in the data are key considerations for defining a detectable signal. For this time-lapse monitoring approach, both static and dynamic noises were added to the data, based on what has been encountered on average for land acquisition. Both sets of synthetic shot gathers, without and with noise, were run through standard velocity analysis to determine interval velocities for normal move-out corrections and Kirchhoff time migration. Figures 3a-3d show the time-lapse differences between the response when the CO_2 plume was present and the initial conditions for 30 m thick plumes of CO_2 with 20% saturation at depths of 500, 800, 1000, and 1300 m. While the accumulations at 500 and 800 m depths are detectable, at 1000 and 1300 m depths, the response is of the same order as the noise. It may be difficult to ascribe a meaningful change in the section unless the SNR ratio is improved.

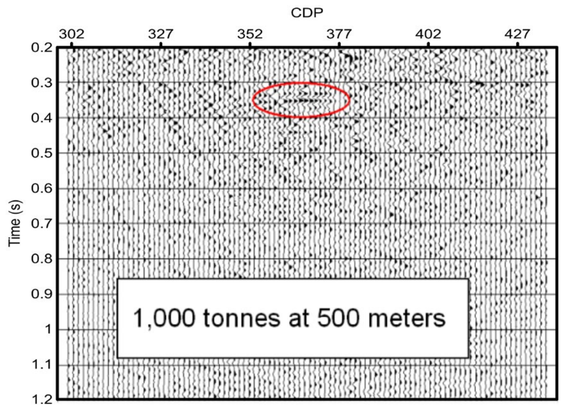

(a)

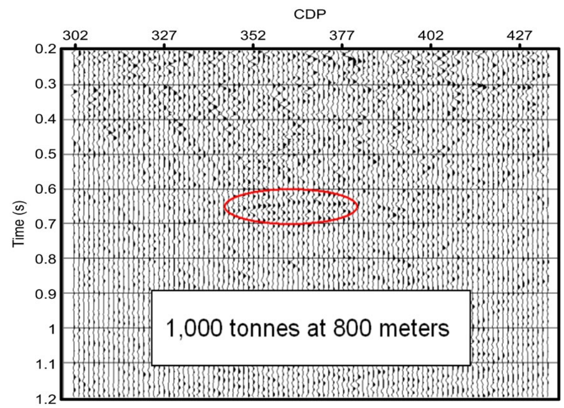

(b)

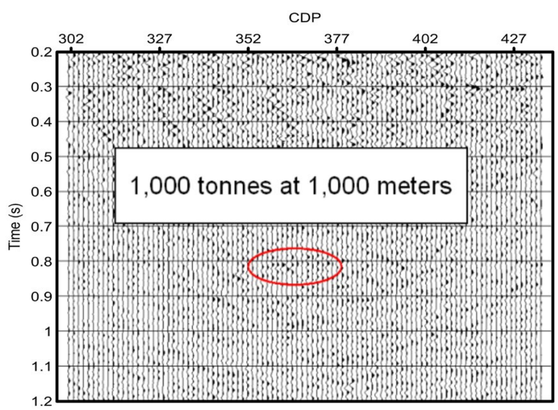

(c)

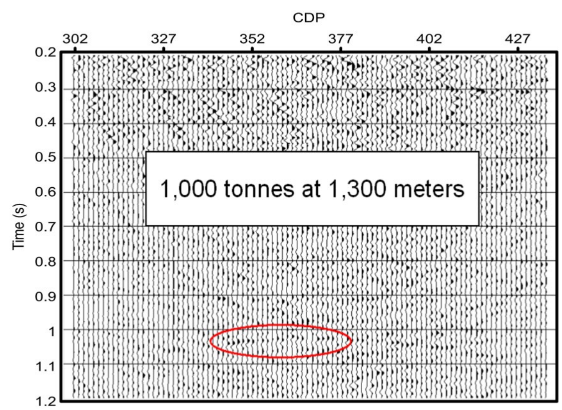

(d)

Figure 3. Differences between migrated sections for the initial conditions and 1,000 tonne CO_2 accumulations at depths of (a) 500 m, (b) 800 m, (c) 1000 m, and (d) 1300 m. A saturation of 20% and 30-m thickness of the cone-shaped accumulation is used for these calculations. The seismic response for the accumulation at depths of 500 and 800 m is detectable; however, the response of the accumulation at depths of 1000 and 1300 m is in the noise level of the survey.

2.2 Physics-based simulated model: Kimberlina-2

The second set of model scenarios was based on a 3D model of the Kimberlina site in the southern San Joaquin Basin, California, simulating a commercial-scale GCS using the TOUGH2-MP/ECO2N simulator (Pruess, 2004; Zhang et al., 2008). In the version of this model known as Kimberlina-2, the hypothetical injection well was ~3 km away from a steeply dipping fault. CO_2 was injected at a rate of 2.5 Mt/year for 60 years. Because of CO_2 buoyancy and local geology, the primary CO_2 plume develops up-dip in the storage reservoir and along the fault that acts as a hydraulic barrier laterally, after CO_2 injection stops. It takes approximately 40 years for CO_2 in the reservoir to reach the fault, and then CO_2 migrates along the fault up-dip to the southeast.

At an arbitrary time after the end of the injection, changes in the fault permeability through leaky windows (high-permeability zones) were introduced to allow for the migration of CO_2 from the reservoir to secondary formations above the reservoir. The deepest secondary formation, the Olcese Formation, is located between 1100 and 1600 m in depth (because of steeply dipping strata) and is the focus of this study. The middle one, the Santa Margarita Formation, lies between 600 and 1200 m in depth, and the shallowest formation, the Etchegoin Formation, is located between 200 and 500 m in depth. The secondary plumes were under the supercritical CO_2 conditions in the lower two zones and the gas phase conditions in the uppermost zone. Modeling scenarios included the secondary CO_2 plume in one of these three formations (Figure 4a) or plumes in all of them simultaneously (Figure 4b). We define the region containing the reservoir and formations above, including the secondary seal, as the storage complex. Hence, the CO_2 plume in the Olcese Formation would be within the storage complex but outside of the storage reservoir. These models were used to evaluate the capability of seismic and EM techniques to detect deep CO_2 plumes in complex geology.

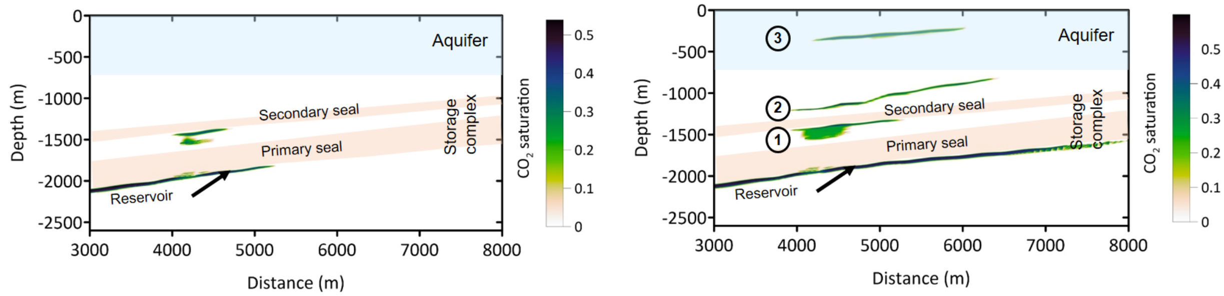

(a) (b)

Figure 4. CO_2 saturation cross-sections for a scenario with (a) a single secondary CO_2 plume in Olcese Formation and (b) three secondary CO_2 plumes present in the (1) Olcese, (2) Santa Margarita, and (3) Etchegoin formations. The secondary CO_2 plume in Olcese Formation is within the storage complex.

A 2D line through the CO_2 plume location along the W-E direction was extracted and used to generate synthetic surface seismic reflection data with a vertical-force point source. The synthetic data consisted of 183 shots and 183 receivers with a 60-m source-receiver interval and a 6.6-km maximum recording offset. The source time function was a 20-Hz Ricker wavelet for computational efficiency. The source in the field usually emits seismic waves with a bit higher frequencies into the Earth. That higher frequency data would result in images with a higher spatial resolution. Three-component data were simulated to a 6.2-s two-way travel time using a high-order, finite-difference, elastic-wave modeling algorithm. Least-squares elastic reverse-time migration (LSRTM) was used to invert for the images of P- and S-wave velocities and density by minimizing the waveform difference between the synthetic and predicted data (Duan et al., 2017; Feng and Schuster, 2017). The time-lapse differences were calculated between inversion models with CO_2 plume and baseline conditions (no CO_2 plume).

As discussed for the previous model, the capability of seismic imaging to locate secondary CO_2 plumes using seismic data depends on the noise levels in the data. We also added seismic noise extracted from a field surface seismic dataset acquired at Kevin Dome, Montana (Clochard et al., 2018), to the synthetic reflection data. We then performed elastic LSRTM using both noise-free and noisy synthetic data with different SNR levels.

Figure 5 shows an example of such a time-lapse difference: The actual P-wave velocity difference in the model is depicted in Figure 5a, the normalized difference in P-wave velocity image using noise-free data is displayed in Figure 5b, SNR=5 is shown in Figure 5c, and SNR=2 is shown in Figure 5d. The estimated location of the secondary plume agrees very well with the actual model, even though the image contains some artifacts, particularly for noisy data. These results illustrate the capability to locate deep CO_2 plumes using surface seismic data and advanced seismic imaging. Similar results were obtained for shallower plumes and models with multiple plumes (not shown).

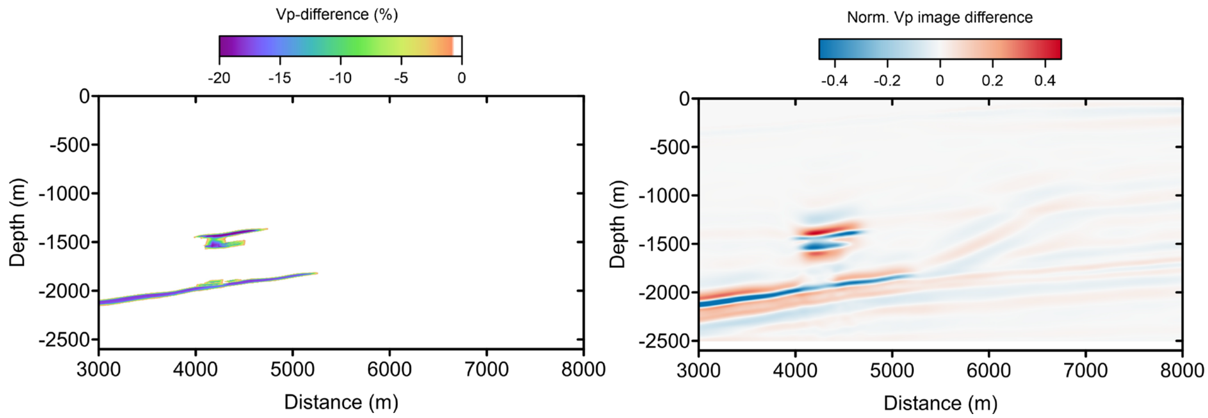

(a) (b)

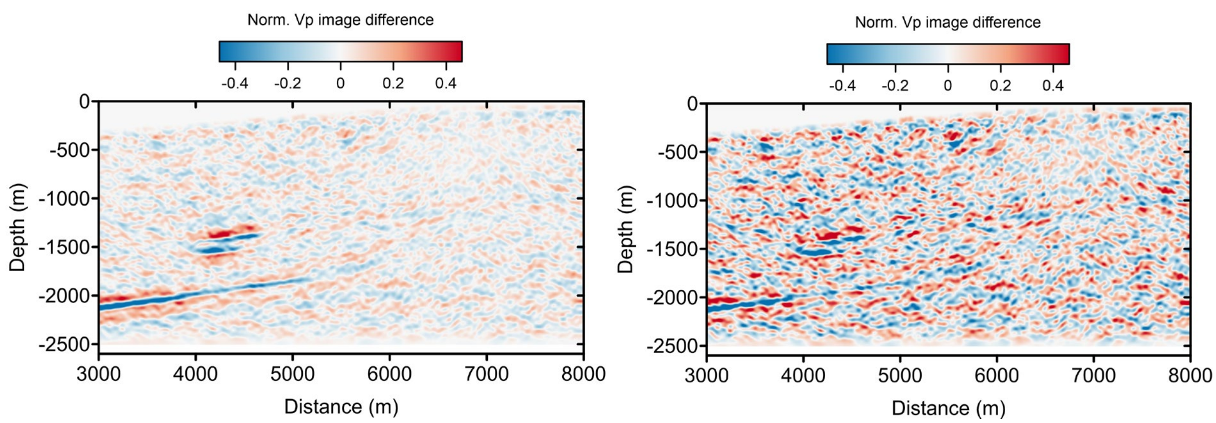

(c) (d)

Figure 5. (a) Actual model P-wave velocity difference for a CO_2 plume at 1500-m depth, and normalized P-wave velocity image difference using (b) noise-free data, (c) noisy data with SNR=5, and (d) noisy data with SNR=2. The estimated location of the secondary plume in (b) and (c) agrees very well with the actual model (a); with significant noise in the data (d), the detection capabilities degrade.

Seismic migration imaging is a stacking process to improve the SNR of the seismic image compared with the SNR of seismic data. In simple common-mid-point (CMP) stacking, the SNR can theoretically be improved by a factor of $\sqrt{N}$, where N is the trace number for CMP stacking (Yilmaz, 2001; Dai, 2012). Hence, the migration image should have a higher SNR than the SNR of the seismic data.

Since the detectability of a secondary CO_2 plume strongly depends on the seismic data acquisition geometry, we further study the seismic imaging capability with sparser and shorter offset acquisition geometry using noisy data with data SNR=2. This study would be appropriate when evaluating whether seismic acquisition costs could be reduced. We performed seismic simulation and imaging with 183, 157, 138, 122, 110, and 100 receivers/shots uniformly distributed on the surface (fixed 6.6-km maximum recording offset). Figure 6 provides an image of SNR versus $\sqrt{N}$ (red dots), where N is approximated by the total recorded trace number. Sparser receivers/shots decrease the quality of seismic image, and the ratio of image SNR to $\sqrt{N}$ is approximately constant (indicated by the dashed black curve in Figure 6). The quality of a seismic migration image also depends on the recording offset of the acquisition geometry. We also performed seismic modeling and imaging for 5.5-, 4.4-, 3.3- and 2.2-km maximum recording offsets (fixed 60-m receiver/shot intervals) (blue dots in Figure 6). A shorter offset decreases the quality of seismic image, and the ratio of image SNR to $\sqrt{N}$ is mostly the same constant as sparser receivers/shots (dashed black curve).

This approximate relationship can be used to help determine whether a denser or longer-offset acquisition geometry is worth the increase in seismic image quality. We do not give the value of constant for approximating the ratio of image SNR to $\sqrt{N}$ because this value depends on a specific model, in addition to source and acquisition types. Note that the relationship is not valid if the acquisition geometry is too sparse and generates strong aliasing artifacts in migration images. It is also not valid if the acquisition geometry has a very short offset, as shown by the blue dot at the bottom right of Figure 6 for 2.2-km maximum recording offsets. The reason is that our synthetic seismic data record very weak S-wave events at near offsets. In addition, seismic traces recorded at large and small offsets are usually different in field data.

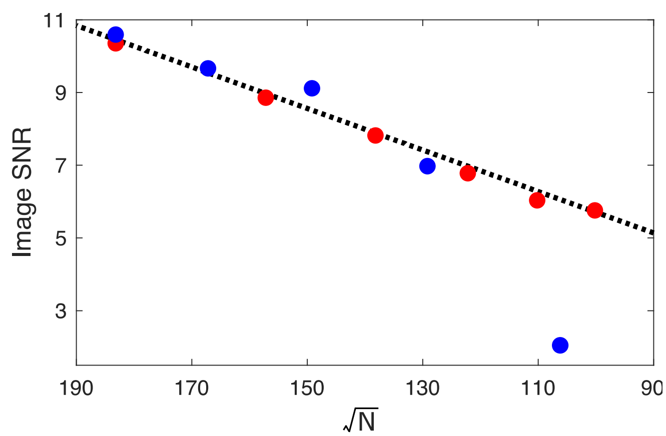

Figure 6. Image SNR versus $\sqrt{N}$ for acquisition geometry with sparser receivers/shots (red dots) and shorter recording offsets (blue dots). The dashed black curve is for image SNR to $\sqrt{N}$ = C, where C is a constant factor.

3. Electrical and electromagnetic monitoring

3.1 Resistivity response to CO_2

Thanks to commercial interest in large-scale GCS projects, another peak in EM applications and inclusion in monitoring packages is possible. Electrical and EM techniques are complementary to seismic or gravity methods because they are sensitive to changes in fluid properties. The goal of time-lapse monitoring is to identify changes in resistivity caused by a CO_2 plume displacing

(ρ_b) of the subsurface

depends on formation properties such as porosity (ϕ), pore fluid resistivity (ρ_w), and fluid saturation (S_w). Furthermore, pore fluid resistivity depends on total dissolved solids (TDS) and temperature, as shown in Figure 7a—the higher the TDS or temperature values, the lower the pore fluid resistivity. Archie's law (Archie, 1942) is one of several empirical relationships linking sedimentary rock formations and electrical properties:

$$\rho_b = a\,\phi^{-m}\,\frac{\rho_w}{S_w^n}$$

where a is tortuosity and m and n are constants, with $1.8 < m \leq 2$ and $n \cong 2$.

When a formation contains a substantial amount of clay, other site-specific rock physics models should be used. Figure 7b shows the rock bulk resistivity (ρ_b) as a function of CO_2 saturation ($1\text{-}S_w$) for the formation with brine resistivity of 0.33 Ohm-m and porosities from 20% to 50%. The replacement of saline fluids (low resistivity) with CO_2 (high resistivity) in deep saline formations increases the resistivity. In shallow aquifers, dissolved CO_2 decreases fluid resistivity, but gas-phase CO_2 increases formation resistivity. These two opposite effects cancel each other out to a certain extent, but dissolved CO_2 has a more significant impact on formation resistivity, which results in an overall decrease in formation resistivity (Yang et al., 2015).

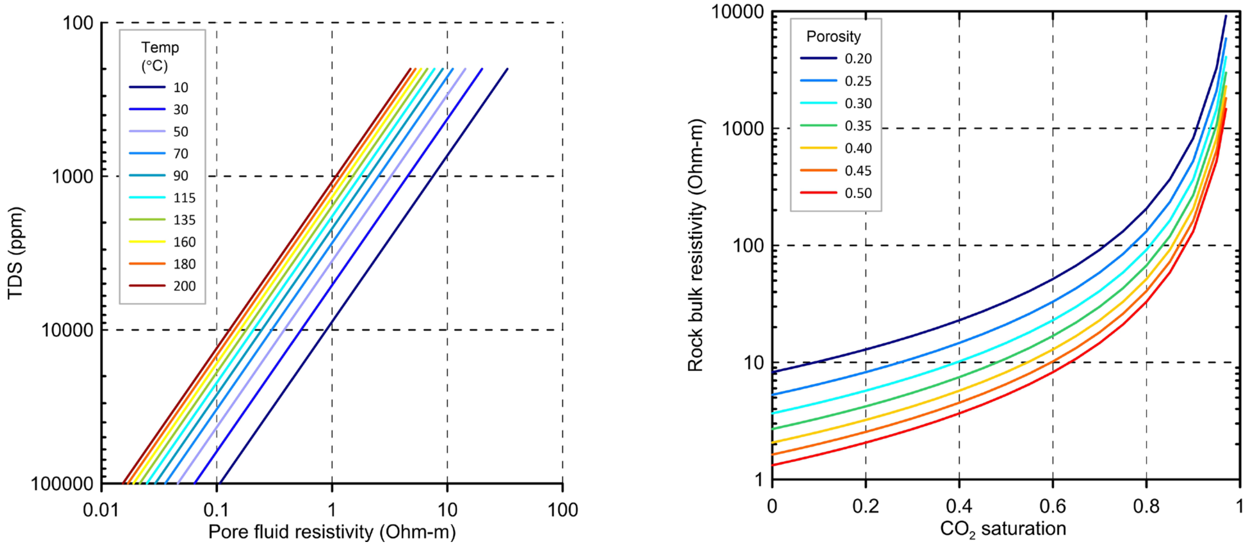

(a) (b)

Figure 7. (a) Pore fluid resistivity as a function of TDS and temperature shown in color; (b) rock bulk resistivity (ρ_b) as a function of CO_2 saturation and porosity (ϕ) (shown in color). Pore fluid resistivity is 0.33 Ohm-m, a =1, m = 2, and n=2. Pore fluid resistivity decreases with increasing TDS or temperature. Rock bulk resistivity increases with CO_2 saturation and decreases with porosity.

When monitoring is designed for detection of secondary CO_2 plumes, it is expected that CO_2 saturations would be at the lower end, which supports high sensitivity of resistivity to CO_2 saturation changes.

Surface resistivity surveys have been used extensively for monitoring in the upper 600 m in depth. Figure 8 illustrates the rapid decrease in the response change due to CO_2 presence, with an increasing target depth for such techniques.

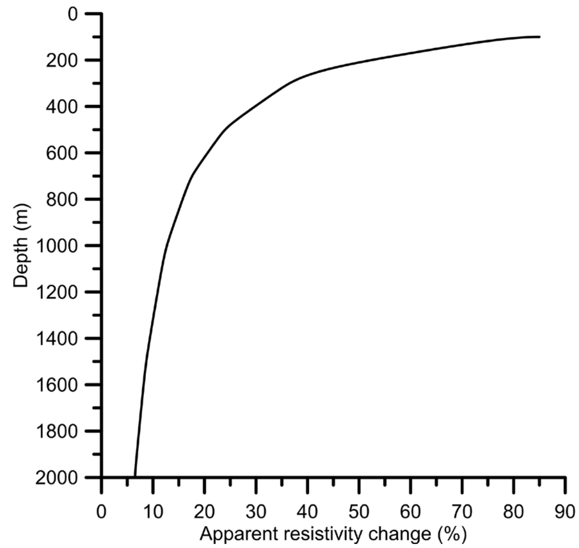

Figure 8. Apparent resistivity changes as a function of target depth for surface resistivity techniques. The response due to CO_2 presence decreases with an increasing target depth.

3.2 Kimberlina-2: Surface and borehole-to-surface EM monitoring

To evaluate the feasibility of using CSEM for time-lapse monitoring of deep plumes, numerically simulated CO_2 plumes using the Kimberlina-2 model (see Section 2.2 for the model description) were used. Both surface and borehole-to-surface configurations were considered (Figure 9). For surface configurations, both transmitters and receivers were on the surface (Figure 9a). For borehole-to-surface arrays, transmitters were in a borehole and receivers were on the surface (Figure 9b). Surface configurations were only sensitive to shallow features (e.g., plume (3) in Figure 9a) and detected only the shallowest secondary CO_2 plumes (red curve in Figure 9c). Borehole-to-surface configurations, where the transmitter position was optimized for zones of interest, were more sensitive to deeper plumes and hence are feasible for time-lapse monitoring and detection of CO_2 plumes at various depths (Figure 9d).

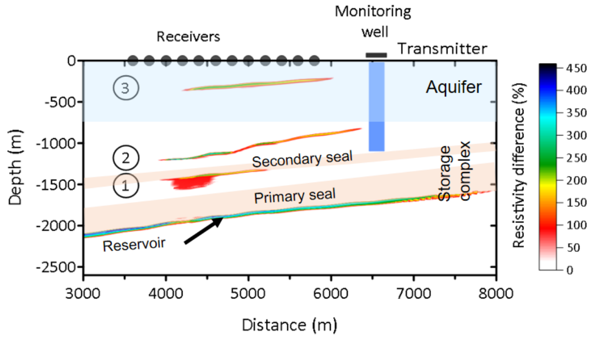

(a)

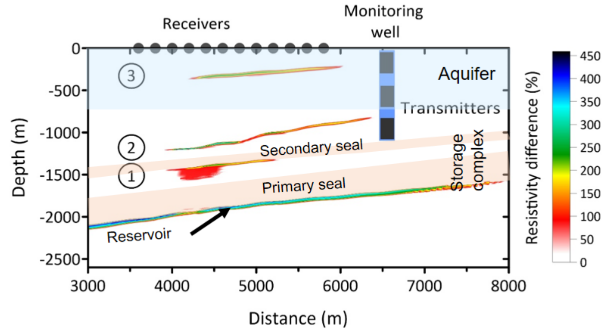

(b)

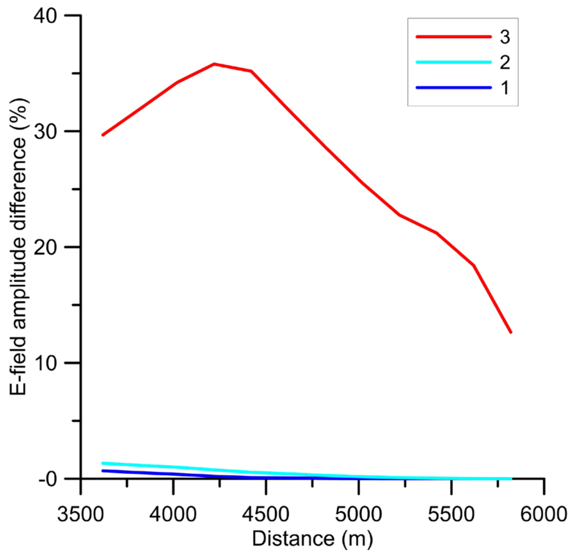

(c)

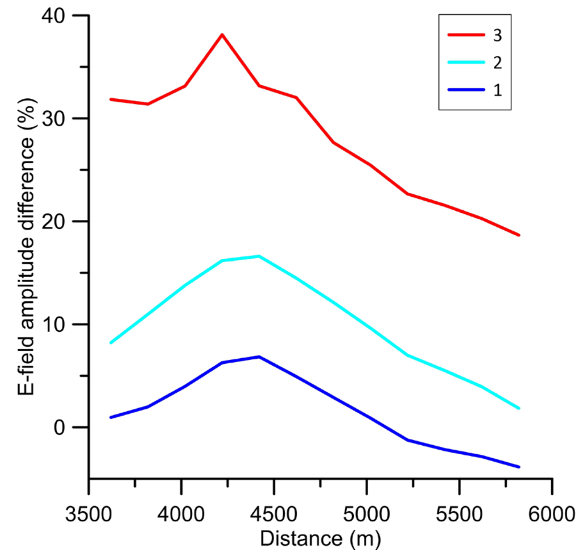

(d)

Figure 9. A model with CO_2 plumes at three different depths: (1) 1500 m, (2) 1000 m, and (3) 300 m with (a) surface array and (b) borehole-to-surface array. Receivers are shown as black circles and transmitters are shown as black rectangles. The difference in electric field amplitude for (b) surface array and (c) borehole-to-surface array due to CO_2 plumes shown in (a) and (b).

When the objective is to monitor deep secondary CO_2 plumes (Figure 10), the measured signal must be above the detection threshold for tracking the plume with time (Figure 10c). The detection threshold was selected based on field experience from past EM surveys. This value would be established based on site-specific field conditions. As illustrated in Figure 10a, CO_2 initially migrates into two separate layers of the formation (yellow outline in Figure 10a), and the difference in electric field amplitude (yellow curve in Figure 10c) caused by these two CO_2 accumulations is within the noise level. Hence, EM would not be effective at detecting these separate CO_2 plumes. Once the CO_2 fills the formation (magenta outline in Figure 10a) and forms one plume, the difference in the electric field amplitude (magenta curve in Figure 10c) is clearly above the detection threshold and indicative of CO_2 plume presence. Under favorable conditions, the plume could be detected at t_1+5 years. As the CO_2 plume grows, the time-lapse difference in electric field amplitude increases (magenta, blue, and green lines in Figure 10c). The changes in subsurface resistivity caused by CO_2 presence for time t_1+ 40 years are shown in Figure 10b. This example illustrates that optimizing transmitter and receiver positions in the monitoring array allows the measured signal from the zones of interest to be maximized. These fit-for-purpose CSEM monitoring arrays would be suitable for monitoring over large areas, although they have yet to be tested at actual sites.

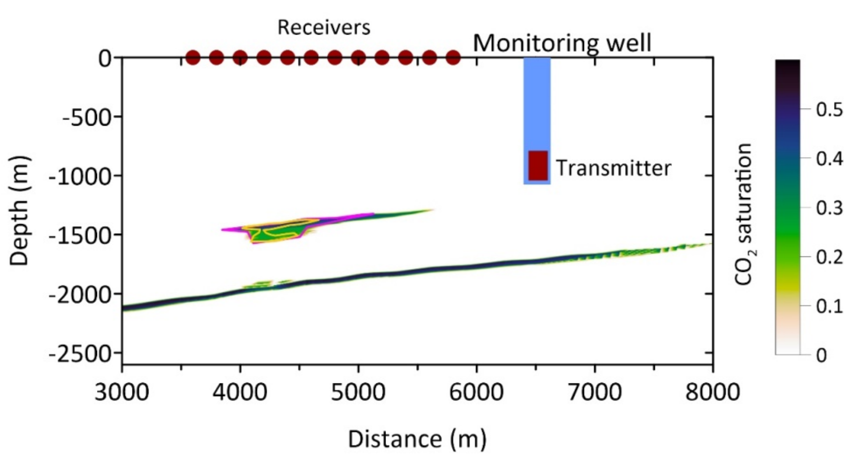

(a)

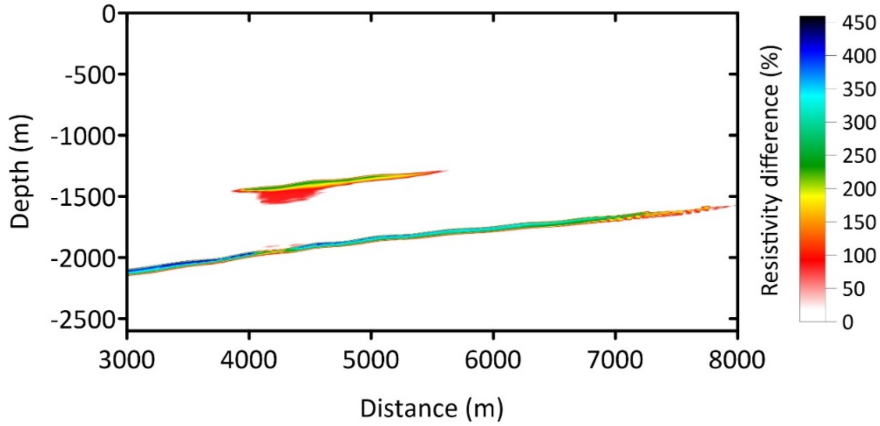

(b)

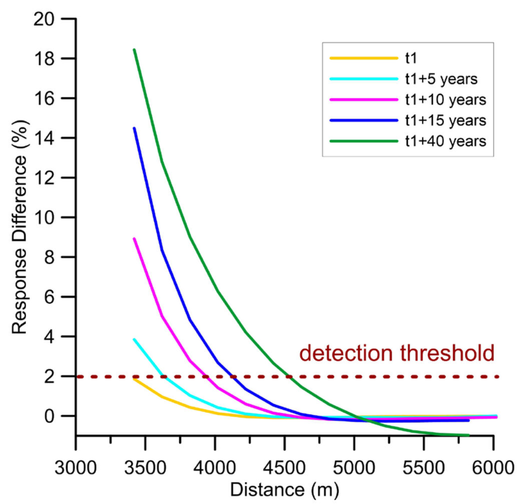

(c)

Figure 10. (a) The model with CO_2 plume at 1500-m depth: receivers are shown as red circles, the transmitter is shown as a red rectangle; (b) changes in subsurface resistivity due to CO_2 presence at t1+40 years; and (c) difference in electric field amplitude at t_1, t_1+5, t_1+10, t_1+15, and t_1+40 years using borehole-to-surface EM configuration (t_1 is the time of the seismic survey shown in Figure 5).

4. Gravity monitoring

4.1 From multi-physics models to simplified approaches

Multi-physics models are important for integrating the geological complexity of a storage site. When planning gravity surveys, consideration should be given to the extent and expected magnitude of the predicted anomaly associated with the CO_2 migration in the subsurface. Appriou et al. (2020) used Kimberlina-2 models (described in Section 2.2) to evaluate the performance of time-lapse gravity monitoring to detect CO_2 accumulations. They found that calculations using an analytical solution for a vertical cylinder model were a good first-order approximation of responses from multi-physics Kimberlina-2 models to evaluate the gravity response associated with the presence of secondary CO_2 plumes. This approach could be used in the early stages of GCS site evaluation when subsurface properties are subject to considerable uncertainty. Multiple simple models based on this approach were used in this study to assess the feasibility of gravity monitoring and identify the conditions required to detect potential secondary CO_2 accumulations.

The gravity signal is directly influenced by the change in bulk density. The bulk density change, Δd, associated with the CO_2 migration in the subsurface can be expressed as (Eiken et al., 2008; Jacob et al., 2016):

$$\Delta d = \Delta S_{CO_2} \phi \left(d_{CO_2} - d_{brine}\right)$$

where ΔS_{CO_2} is the change in CO_2 saturation, and considering here that porosity changes are negligible. This statement can be subject to discussion as porosity changes may be observed but are usually limited to the near-wellbore region, where fluid-rock interaction may lead to dissolution, such as in carbonate formations (Seyedi et al., 2020). Also note that ground surface deformations caused by injection-induced pore pressure increase and the subsequent geomechanical response of the storage complex have been observed at onshore sites (Vasco et al., 2010; Mathieson et al., 2011) and were recently discussed in Kabirzadeh et al. (2020) to evaluate the impact of surface deformation on the gravity response. Geodetic measurements are usually integrated into the monitoring program of GCS sites so that the effects of surface displacement can be removed from the observed gravity response to obtain gravity changes related exclusively to the density changes associated with CO_2 injection.

The accuracy of gravity measurements depends on the sensitivity of instruments and whether the surveys are conducted on land or at sea, at the surface, or in a borehole. The most recent land superconductive gravimeters have a precision of 1 μGal (10^{-8} m/s^2) (Van Camp et al., 2016). Various corrections of gravity measurements impact the accuracy and repeatability of gravity surveys. Reported errors associated with time-lapse gravity measurements are 5 μGal (Jacob et al., 2010), and measurements repeatability about 1 μGal for gravity anomaly larger than 10 μGal (Furre et al., 2017). Borehole gravimeters are also relative instruments, and recent gravity borehole surveys have reached an accuracy of 2.6 μGal and a repeatability of 5.4 μGal (Bonneville et al., 2021). A complete discussion of various sources of uncertainties and noise in gravity measurements—beyond the scope of this paper—is presented in Van Camp et al. (2017). This range of detectability was used in the approach presented below to assess the detectability of secondary CO_2 plume.

4.2 Surface gravity

Surface gravity sensitivity was investigated with a conceptual model that assumes CO_2 moves out from the storage reservoir, accumulates in a secondary trap above the storage horizon, and forms a cylinder-shaped plume. Realistic subsurface conditions, close to those encountered at the Kimberlina site, were used to calculate CO_2 density. A hydrostatic pore pressure gradient of 10.5 kPa/m, a geothermal temperature gradient of 26.8°C/km, a surface temperature of 21.8°C, and a porosity of 34% were used. The cylinder height was assumed to be 30 m, the radius varied from 500 to 3000 m, and CO_2 saturations ranged from 5% to 60%. The gravity effect of each vertical cylinder considered was determined using the analytical solution given by Telford (1976).

CO_2 plume size (cylinder radius) required to produce a signal of -4 μGal is plotted as a function of depth and CO_2 saturation (Figure 11a) and CO_2 mass (Figure 12a). Figures 11b and 12b show these relationships for the signal of -10 μGal. Note that an inflection of all curves around 800 m corresponds to a significant change in CO_2 density linked to the transition to a supercritical state. Also, the curves tend toward an asymptote, making it more challenging to determine the correct CO_2 mass at great depths.

These figures can be used to quickly determine the conditions (i.e., depth, mass, extent, CO_2 saturation) under which a secondary plume can be detected by a surface gravity survey for a given signal level at a site with characteristics similar to those described above. The results clearly show that the extent (radius) of the plume controls the depth at which this plume would be detectable for a given CO_2 mass and a given signal threshold. Increasing the plume radius or CO_2 saturation increases the depth of a detectable plume, i.e., the signal response reaches a defined threshold. The CO_2 mass increases with plume size and depth. For example, in Figure 11a, a plume of 500-m radius and 20% CO_2 saturation would be detectable at a depth of 750 m, while for a 1000-m radius and the same CO_2 saturation, the depth would be 1000 m. In Figure 12a, for a detection threshold of -4 μGal, a 10,000-tonne CO_2 secondary plume with a radius of 500 m can be detected at a depth of 300 m, but the plume mass would need to be about 1,000,000 tonnes to be detected at a depth of 1200 m. If this threshold is set at -10 μGal (Figures 11b and 12b), the 10,000-tonne and 1,000,000-tonne CO_2 plumes would only be detected at shallower depths, 200 and 900 m, respectively.

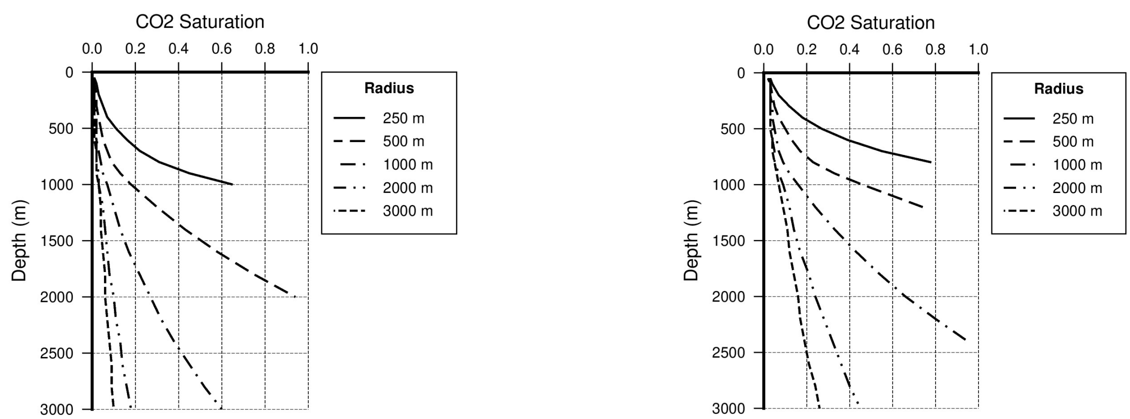

(a) (b)

Figure 11. CO_2 plume size (cylinder radius) as a function of CO_2 saturation and depth to produce a signal of (a) -4 μGal and (b) -10 μGal. The radii of 250, 500, 1000, 2000, and 3000 m are shown as solid, dashed, dot-dashed, double dot-dashed, and dotted lines, respectively. The deeper the plume, the larger the size or CO_2 saturation required to produce the same signal measured on the surface.

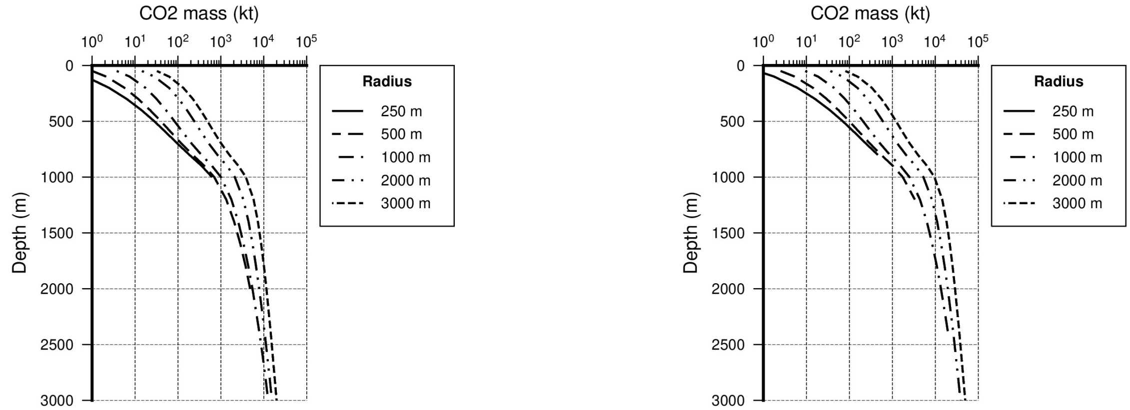

(a) (b)

Figure 12. CO_2 plume size (cylinder radius) as a function of CO_2 mass and depth to produce a signal of (a) -4 μGal and (b) -10 μGal. The radii of 250, 500, 1000, 2000, and 3000 m are shown as solid, dashed, dot-dashed, double dot-dashed, and dotted lines, respectively. The CO_2 mass increases with plume size and depth. The curves asymptote and make it difficult to determine the correct CO_2 mass at great depths.

Figures 13a and 13b show the plume radius as a function of depth for variable CO_2 saturations for the signal levels of -4 μGal and -10 μGal, respectively. These figures clearly illustrate the relationship between CO_2 saturation and the plume depth and size: The higher the saturation, the greater the depths of detection for a given radius of the CO_2 secondary plume or smaller size.

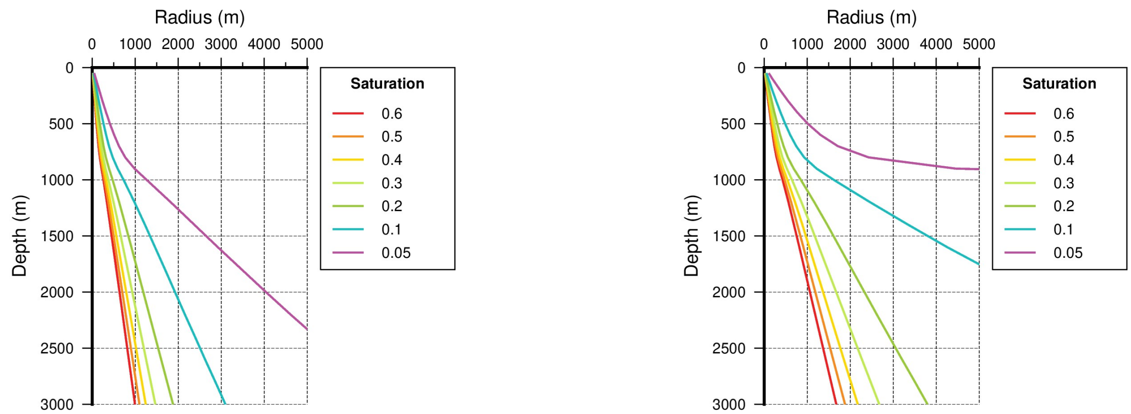

(a) (b)

Figure 13. CO_2 plume radius as functions of depth for a variable CO_2 saturation (shown in color) for signal levels of (a) -4 μGal and (b) -10 μGal. The higher the saturation and the larger the plume size, the greater the depth of detection.

The expected gravity responses described here were compared with the performance of the seismic and EM methods applied to the Kimberlina-2 models (Sections 2.2 and 3.2). The gravity signal expected at a given depth (e.g., 1500 m) for cylinders of increasing radius and CO_2 saturation was computed for this comparison. Multiple cylinders can be used for more complex CO_2 accumulations, such as those developed in the Olcese Formation. In this example, these plumes were modeled using two cylinders and their respective properties (i.e., depth, porosity, CO_2 saturation, thickness, lateral extent). The corresponding gravity signals for each time step considered (t_1, t_1+5, t_1+10, t_1+15 years, and t_1+40 years) were calculated and are plotted in Figure 14. This figure shows that the CO_2 accumulation in the Olcese Formation is detectable at t_1+10 years with a detection threshold of -4 μGal and at t_1+40 years with a detection threshold of -10 μGal. Depending on the noise level, or the detection threshold, CO_2 accumulation at a depth of

1500 m in the Kimberlina-2 model (Figures 4a, 5a, and 10) would be detectable by surface gravity at the same time as the EM technique. This is consistent with results presented in Appriou et al. (2020), where a forward modeling approach was applied on the Kimberlina-2 model.

These models could be adapted to any desired threshold and site-specific parameters to provide the conditions at which a secondary CO_2 plume would be detectable with surface gravity measurements.

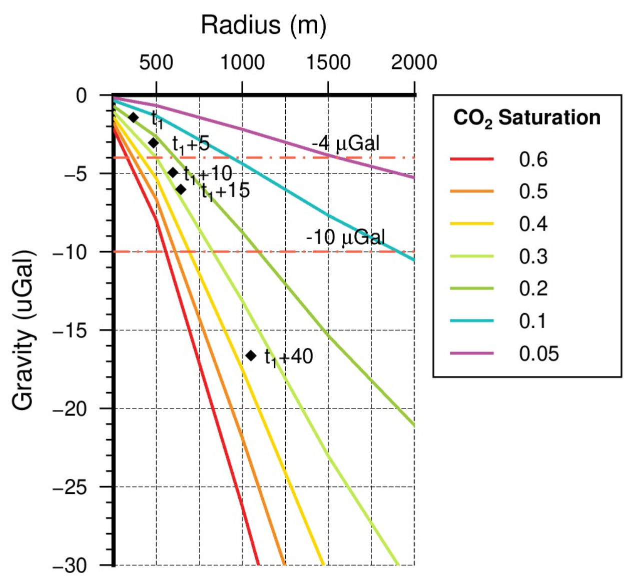

Figure 14. Evolution of the gravity response for a CO_2 accumulation occurring at a depth of 1500 m, with increasing radius and variable CO_2 saturation. Two dashed red lines represent the detection thresholds of -4 μGal and -10 μGal. Black diamonds at t_1, t_1+5, t_1+10, t_1+15, and t_1+40 years correspond to the simplified two-cylinder model used to approximate the secondary plumes shown in Figure 10a (t_1 is the time of the seismic survey shown in Figure 5).

4.3 Borehole gravity

Gasperikova and Hoversten (2008) show that a 1% change in density of a CO_2 wedge of a 250-m radius and 20% CO_2 saturation, within a 100-m-thick sand layer of 20% porosity at a depth of 1000 m, produces a -10 μGal response at the edge of the plume and decreases to -2.5 μGal at 200 m from the edge. In the present study, the range of models was expanded and the feasibility of borehole gravity monitoring was investigated using a simple prism model (Figure 15). The CO_2 plume was represented by a prism of constant 20-m thickness with varying depth and horizontal dimensions and the same initial conditions as those used for the surface measurements. Scenarios included CO_2 mass from 10,000 to 500,000 tonnes, bulk density changes from 1% to 5%, and prism depths from 100 to 3000 m. The volume of the prism—accommodated by changes in horizontal dimensions—depends on the CO_2 mass and the CO_2 density at the prism depth.

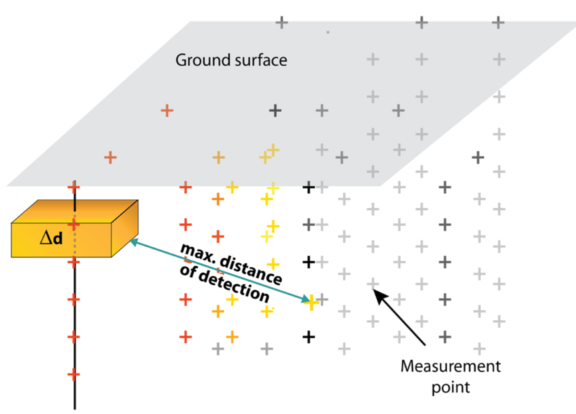

Figure 15. A conceptual model for borehole gravity calculations. The 3D prism with Δd density contrast represents the CO_2 plume, for which depth and horizontal dimensions can vary; plus symbols indicate measurement locations.

For each value of the CO_2 mass, bulk density, and depth of the prism, the gravity anomalies at each node of a 3D grid were computed using Dubey and Tiwari's (2016) algorithm. Then, the maximum distance from the edge of the prism at which one of the gravity components (horizontal or vertical) reached a given signal response (-5 and -10 μGal) was determined. Figures 16 and 17 plot the maximum distance at which a CO_2 plume triggers a gravity response in the vertical (g_z) component as a function of the prism depth for different density changes, masses, and for -5 and -10 μGal responses, respectively. The distances using the horizontal component (not shown) are slightly smaller. To detect deep CO_2 plumes, the borehole measurements would have to be taken within 20 to 700 m of the edge of the CO_2 plume, depending on the CO_2 mass (volume) and the density change. At shallow depths, the detection of plumes becomes easier because of the significant change in the CO_2 density occurring at ~800 m and can reach up to 3000 m away for the largest CO_2 plume considered here (500,000 tonnes).

The mass of the CO_2 plume and the bulk density change caused by the plume are fundamental for its detection. As shown in Figure 16, for a gravity response of -5 μGal and a CO_2 plume bulk density change from 1% to 5%, the detection distance will range from 40-70 m to about 400-700 m for a CO_2 mass of 10,000 and 500,000 tonnes, respectively.

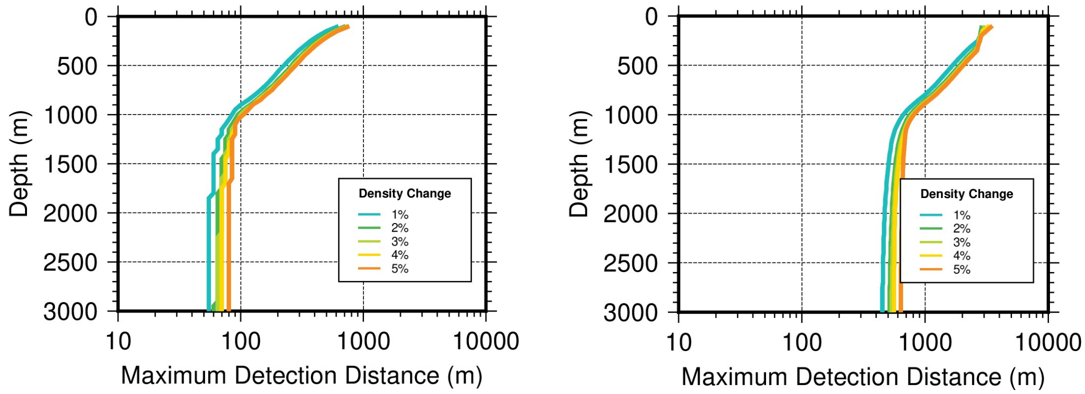

(a) (b)

Figure 16. Maximum distance of detection vs. depth of a -5 μGal change in the vertical gravity component g_z for (a) 10,000 tonnes and (b) 500,000 tonnes. CO_2 mass and bulk density changes varying from 1% to 5% are shown in color.

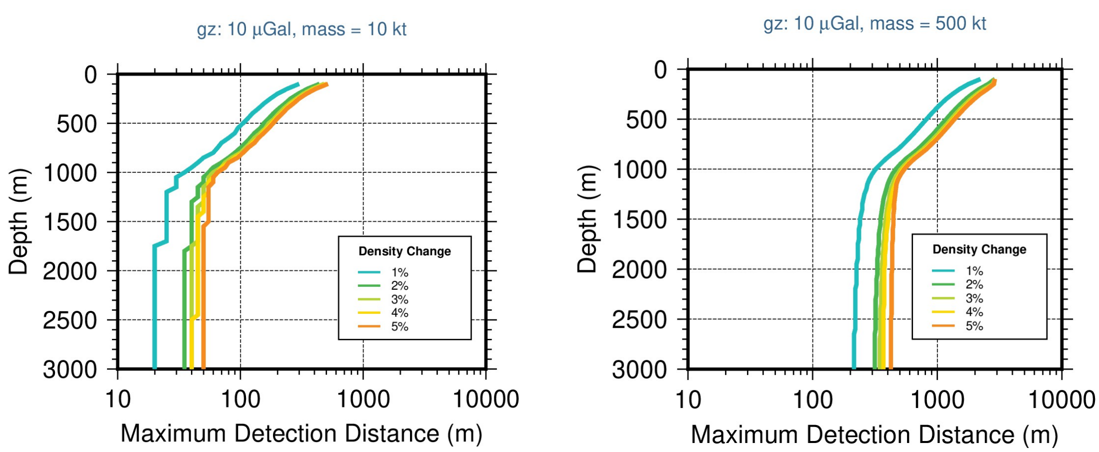

(a) (b)

Figure 17. Maximum distance of detection vs. depth of a -10 μGal change in the vertical gravity component g_z for (a) 10,000 tonnes and (b) 100,000 tonnes. CO_2 mass and bulk density changes varying from 1% to 5% are shown in color.

5. Evaluation of monitoring in the post-injection phase

Figure 18 shows factors that influence the final monitoring design: (1) required accuracy and resolution, (2) detection thresholds, (3) sensitivities of considered technologies, (4) required spatial and temporal sampling, (5) costs, (6) risk profile or risk uncertainty at a site, and (7) value of information (the cost of additional information a decision-maker would be willing to pay before making a decision). If a monitoring configuration needs to fulfill multiple objectives, it has inherent trade-offs (e.g., less resolution for one objective vs. unnecessary resolution and associated high cost for another objective). This trade-off may result in the unsatisfactory performance of such a design. In this study, we work with the idea of an adaptive monitoring framework, in which reservoir monitoring and post-injection monitoring for secondary CO_2 plumes would be designed separately for their respective objectives. Reservoir monitoring using seismic methods in the post-injection phase is still a subject of active research (e.g., Lumley, 2021). We focus on two components of this puzzle: the sensitivities and detection thresholds of seismic, EM, and gravity methods that could play an important role in post-injection monitoring for secondary CO_2 plumes. This study also addresses one of the recommendations from the IEA Greenhouse Gas R&D Programme (IEAGHG, 2020) to establish thresholds and forward modeling approaches to design monitoring configurations.

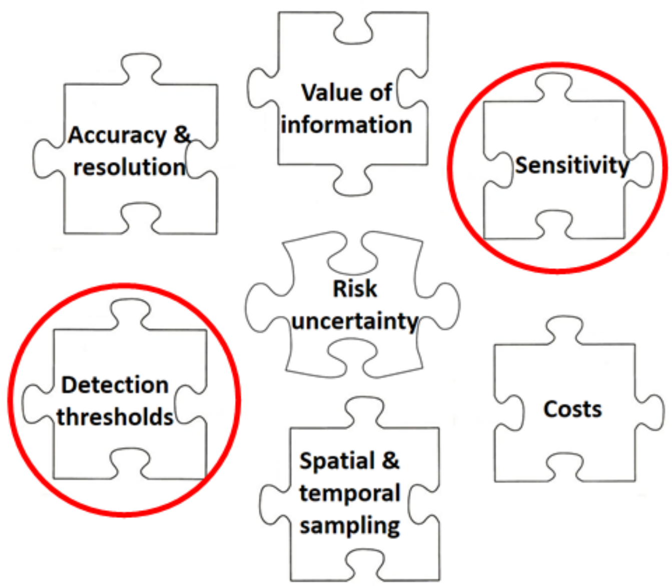

Figure 18. Factors influencing a monitoring design at a GCS site.

Identification of areas where post-injection monitoring costs would be less than possible mitigation costs from an unwanted event or public assurance would be carried out as part of a site risk assessment (e.g., Pawar et al., 2015; Yang et al., 2018b). This would likely require one or multiple monitoring wells close to or in the region with a higher risk. These wells could be considered in the monitoring arrays for source or sensor deployments for geophysical monitoring. It is essential that their locations and specifications are optimized prior to drilling because of the high cost associated with drilling and instrumenting boreholes.

Costs of monitoring technologies have not significantly changed over the last two decades, and costs associated with EM and gravity surveys are typically a fraction of those of 4D seismic surveys, but seismic provides much better resolution than the other two techniques (e.g., Benson et al., 2004; IEAGHG, 2020). Figure 6 illustrates that the capability to detect small plumes decreases with sparser seismic arrays. On the other hand, if the dense arrays used for reservoir monitoring are considered, frequent seismic surveys might be non-economical in the post-injection phase.

Figures 5, 10, and 14 illustrate how complementary techniques could be used in a cost-effective monitoring design. The Kimberlina-2 model demonstrates a realistic scenario. While CO_2 may migrate out of the reservoir, it accumulates in the formation within a storage complex and as such would not trigger any need for immediate action. The seismic method is sensitive to smaller volumes and low CO_2 saturation (Figure 5) and would detect the plume first, but the seismic survey might not be necessary at that stage. The EM and gravity signals are small (yellow curve in Figure 10c; t_1 in Figure 14); thus, EM and gravity methods would not be effective at this stage. However, as the plume grows, the signal rises above the detection threshold, and EM and gravity methods could be used for monitoring. EM and gravity techniques are also sensitive to higher CO_2 saturation changes at which the seismic technique reaches an asymptotic response (e.g., Kim et al., 2010; Gasperikova and Li, 2021). Having this independent information would be important if there is a need for accurate accounting of CO_2 in the storage complex. It is also important to note that if the same size CO_2 plume was present at shallower depths, the measured EM and gravity signals would be larger (above the detection threshold), and both monitoring methods could be used sooner than in this case.

While site-specific conditions would govern how fast the plume could grow, note that it takes 15 years for the plume to double in size. During the next 25 years, the plume grows by ~500 m laterally, CO_2 accumulates at the formation top, and the volume expands only by ~10%. In such a scenario, frequent monitoring campaigns are not necessary. Time-lapse EM and gravity surveys could be carried out at adaptive intervals driven by site-specific conditions. After a couple of surveys confirming that the secondary CO_2 plume is stable, the interval to the next survey would be increased. However, any signal responses beyond the expected change that would be observed in the time-lapse EM and/or gravity surveys would trigger a need for a seismic survey.

Borehole gravity measurements could detect the presence of deep secondary CO_2 plumes if monitoring wells were relatively close to the plume. This could only be achieved with optimized well locations, limiting the use of the method for early detection in the post-injection phase.

The requirements for arrays to detect a plume are less stringent than those necessary for the plume characterization. These translate directly to survey costs. A cost-effective monitoring framework for the post-injection phase would likely consist of both configurations.

4D seismic monitoring will likely be part of the monitoring strategy in the injection phase of any large-scale projects to track the development of the CO_2 plume in the subsurface for conformance and containment purposes. It may be deployed one last time at the end of the injection phase or at the beginning of the post-injection phase, along with EM and gravity surveys, to provide a baseline for the post-injection monitoring. A cost-effective monitoring strategy in the post-injection phase would use lower cost techniques like EM or gravity to monitor large areas. If an anomaly is detected, a seismic survey could be executed over a much smaller area surrounding this anomaly to further control post-injection monitoring costs. EM or gravity methods will be an integral part of the post-injection monitoring even when new, lower cost approaches to long-term seismic monitoring become a part of a standard monitoring toolbox.

6. Conclusions

This study focuses on assessing detection limits and sensitivities of three primary geophysical monitoring methods (seismic, EM, and gravity) for cost-effective detection of secondary CO_2 plumes that might be formed by CO_2 migrating from a storage formation into zones above the primary reservoir seal in the post-injection phase.

Time-lapse seismic surveys with advanced seismic imaging can locate CO_2 plumes from shallow to deep regions of the GCS site. The detectability of these CO_2 plumes strongly depends on the seismic data acquisition geometry and the noise levels in the data. Sparser receivers/shots or shorter offsets lower the survey costs but decrease the seismic image quality.

EM techniques are sensitive to changes in fluid properties. Deep CO_2 plumes are not detectable by surface measurements, but borehole-to-surface configurations offer increased sensitivity to these plumes. The gravity method is the only geophysical method that can provide a direct estimate of CO_2 mass distribution at depth. The gravity surveys will reveal CO_2 accumulations occurring in the deep subsurface if the mass of CO_2 migrating out of the targeted formation is significant. EM and gravity methods have a lower spatial resolution but provide additional information about the subsurface that complements seismic monitoring.

For all methods, the current state-of-the-art is likely to be improved over time. As greater volumes of CO_2 are injected at large-scale GCS projects, the costs of monitoring technologies per tonne will also decrease. The advancements in seismic and EM techniques presented here can also benefit reservoir monitoring. Future studies should evaluate how to optimally use permeant source and receiver arrays to acquire time-lapse seismic data to increase data repeatability and how to use sparse seismic data for the accurate location of CO_2 plumes. Many simulated gravity responses are not measurable with current instruments but may play an important role in testing or evaluating new technologies on the horizon.

Early detection of any CO_2 accumulations migrating out of the targeted reservoir in the post-injection period is important. Such accumulations, even those significant in terms of CO_2 mass and therefore detectable, would not necessarily pose a risk for the GCS site, as they would remain in the storage complex and deep enough not to jeopardize the protected groundwater.

The seismic method remains a key method to detect CO_2 accumulations for the foreseeable future. However, the current 4D seismic monitoring may be cost-prohibitive and not relevant for a routine deployment in the post-injection phase. Even when lower cost seismic monitoring alternatives for reservoir monitoring are developed, EM or gravity will play an important role in the post-injection monitoring in the deep subsurface. Should a large accumulation be detected with one of these methods, there would be enough time to adapt the monitoring strategy to quantify the significance of these accumulations before mitigation measures are needed, and seismic monitoring would then be critical.

Acknowledgments

This work was completed as part of the National Risk Assessment Partnership (NRAP) project. Support for this project comes from the U.S. Department of Energy (DOE) Office of Fossil Energy's Crosscutting Research Program. Work at Lawrence Berkeley National Laboratory was completed under the U.S. DOE Contract No. DE-AC02-05CH1123. Work at Los Alamos National Laboratory was supported under the U.S. DOE Contract No. 89233218CNA000001. Work at Pacific Northwest National Laboratory was funded under the U.S. DOE Contract No. DE-AC05-

76RL01830. Work at Lawrence Livermore National Laboratory was performed under the U.S. DOE Contract No. DE-AC52-07NA27344 (LLNL-JRNL-820457). We thank the Associate Editor, C. Juhlin, and two anonymous reviewers for their constructive comments and suggestions.

References

Ajo-Franklin, J.B., Peterson, J., Doetsch, J., Daley, T.M., 2013. High-resolution characterization of a CO_2 plume using crosswell seismic tomography: Cranfield, MS, USA. International Journal of Greenhouse Gas Control, 18, 497-509.

Alnes, H., Eiken, O., Stenvold, T., 2008. Monitoring gas production and CO_2 injection at the Sleipner field using time-lapse gravimetry. Geophysics, 73, WA155-WA161.

Alnes, H., Eiken, O., Nooner, S., Sasagawa, G., Stenvold, T., Zumberge, M., 2011. Results from Sleipner gravity monitoring: Updated density and temperature distribution of the CO_2 plume. Energy Procedia, 4, 5504-5511.

Appriou, D., Bonneville, A., Zhou, Q., Gasperikova, E., 2020. Time-lapse gravity monitoring for detecting CO_2 leakage from a faulted subsurface storage complex. International Journal of Greenhouse Gas Control, 95, 102956, https://doi.org/10.1016/j.ijggc.2020.102956.

Archie, G.E., 1942. The electrical resistivity log as an aid in determining some reservoir characteristics. Transactions of the Metallurgical Society of AIME, 146, 54-61.

Baker, S.E., Stolaroff, J.K., Peridas, G., Pang, S.H., Goldstein, H.M., Lucci, F.R., Li, W., Slessarev, E.W., Pett-Ridge, J., Ryerson, F.J., Wagoner, J.L., Kirkendall, W., Aines, R.D., Sanchez, D.L., Cabiyo, B., Baker, J., McCoy, S., Uden, S., Runnebaum, R., Wilcox, J., Psarras, P.C., Pilorge, H., McQueen, N., Maynard, D., McCormick, C., 2020. Getting to Neutral: Options for Negative Carbon Emissions in California. Lawrence Livermore National Laboratory, LLNL-TR-796100, https://www-gs.llnl.gov/content/assets/docs/energy/Getting_to_Neutral.pdf.

Bauer, R.A., Will, R., Greenberg, S.E., Whittaker, S.G., 2019. Illinois Basin – Decatur Project. In: Geophysics and Geosequestration, Davis, T.L., Landro, M., and Wilson, M. (Eds.), Cambridge University Press, pp. 339-369.

Benson, S.M., Gasperikova, E., Hoversten, G.M., 2004. Overview of monitoring requirements for geologic storage projects. Report, IEA Greenhouse Gas R&D Programme.

Bonneville, A., Black, A.J., Hare, J., Kelley, M.E., Place, M., Gupta, N., 2021. Time-lapse Borehole Gravity Imaging of CO_2 Injection and Withdrawal in a Closed Carbonate Reef. Geophysics, 86, 6, 1-20.

Caesary, D., Song, S.Y., Yu, H., Kim, B., Nam, M.J., 2020. A review on CO_2 leakage detection in shallow subsurface using geophysical surveys. International Journal of Greenhouse Gas Control, 102, 103165.

Carrigan, C. R., Yang, X., LaBrecque, D.J., Larsen, D., Freeman, D., Ramirez, A.L., Daily, W., Aines, R., Newmark, R., Friedmann, J., Hovorka, S., 2013. Electrical resistance tomographic monitoring of CO_2 movement in deep geologic reservoirs. International Journal of Greenhouse Gas Control, 18, 401-408.

Chadwick, R.A., Williams, G.A., Falcon-Suarez, I., 2019. Forensic mapping of seismic velocity heterogeneity in a CO_2 layer at the Sleipner CO_2 storage operation, North Sea, using time-lapse seismics. International Journal of Greenhouse Gas Control, 90, 102793.

Clochard, V., DeVault, B.C., Bowen, D., Delepine, N., Wangkawong, K., 2018. Quadri-joint inversion: Method and application to the Big Sky 9C 3D data set in northern Montana. Interpretation, 6, SN101-SN118.

Coueslan, M.L., Ali, S., Campbell, A., 2013. Monitoring CO_2 injection for carbon capture and storage using time-lapse VSPs. The Leading Edge, 32, 1268-1276.

Dai, W., 2012. Multisource least-squares migration and prism wave reverse time migration. The University of Utah.

Daley, T.M., Hendrickson, J., Queen, J.H., 2015. Monitoring CO_2 Storage at Cranfield, Mississippi with Time-Lapse Offset VSP – Using Integration and Modeling to Reduce Uncertainty. Energy Procedia, 63, 4240-4248.

Daley, T.M., Harbert, W., 2019. Goals of CO_2 monitoring: Why and How to Assess the Subsurface Changes Associated with Carbon Capture and Storage. In: Geophysics and Geosequestration, Davis, T.L., Landro, M., and Wilson, M. (Eds.), Cambridge University Press, pp. 54-69.

Dilmore, R., Bacon, D., Brown, C., Harp, D., Gasperikova, E., Oldenburg, C., Pawar, R., Smith, M., Thomas, R., Carroll, S., White, J., Richard, T., 2021. Subsurface Environmental Risks at Geologic Carbon Storage Sites: Perspectives from the U.S. Department of Energy's National Risk Assessment Partnership R&D Experience. Greenhouse Gases: Science and Technology, submitted.

Dodds, K., Krahenbuhl, R., Reitz, A., Li, Y., Hovorka, S., 2013. Evaluating time-lapse borehole gravity for CO_2 plume detection at SECARB Cranfield. International Journal of Greenhouse Gas Control, 18, 421-429.

Duan, Y., Guitton, A., Sava, P., 2017. Elastic least-squares reverse time migration. Geophysics, 82, S315-S325.

Dubey, C.P., Tiwari, V.M., 2016. Computation of the gravity field and its gradient: Some applications. Computers and Geosciences, 88, 83-96.

Eiken, O., Stenvold, T., Zumberge, M., Alnes, H., Sasagawa, G., 2008. Gravimetric monitoring of gas production from the Troll field. Geophysics, 73, WA149-WA154.

Feng, Z., Schuster, G.T., 2017. Elastic least-squares reverse time migration. Geophysics, 82, S143-S157.

Furre, A.-K., Eiken, O., Alnes, H., Vevatne, J.N., Kiær, A.F., 2017. 20 Years of Monitoring CO_2-injection at Sleipner. Energy Procedia, 114, 3916-3926.

Gasperikova, E., Hoversten, G.M., 2008. Gravity monitoring of CO_2 movement during sequestration: model studies. Geophysics, 73, WA105–WA112.

Gasperikova, E., Commer, M., 2019. Electrical and Electromagnetic methods. In: Geophysics and Geosequestration, Davis, T.L., Landro, M., and Wilson, M. (Eds.), Cambridge University Press, pp. 154-167.

Gasperikova, E., Li, Y., 2021. Time-lapse electromagnetic and gravity methods in carbon storage monitoring. The Leading Edge, 40, 442-446.

Girard, J.F., Coppo, N., Rohmer, J., Bourgeois, B., Naudet, V., Schmidt-Hattenberger, C., 2011. Time-lapse CSEM monitoring of the Ketzin (Germany) CO_2 injection using 2xMAM configuration. 10th International Conference on Greenhouse Gas Control Technologies, 4, 3322-3329.

Global CCS Institute, 2020. The Global Status of CCS: 2020. Australia.

Goto, H., Ishido, T., Sorai, M., 2020. Numerical study of reservoir permeability effects on gravity changes associated with CO_2 geological storage: implications for gravimetric monitoring feasibility. Greenhouse Gases: Science and Technology, 10, 557-566.

Gotz, J., Luth, S., Krawczyk, C., Cosma, C., 2014. Zero-Offset VSP Monitoring of CO_2 Storage: Impedance Inversion and Wedge Modelling at the Ketzin Pilot Site. International Journal of Geophysics, Article ID 294717, http://dx.doi.org/10.1155/2014/294717.

Hannis, S., Chadwick, A., Connelly, D., Blackford, J., Leighton, T., Jones, D., White, J., White, P., Wright, I., Widdicomb, S., Craig, J., Dixon, T., 2017. Review of Offshore CO_2 Storage Monitoring: Operational and Research Experiences of Meeting Regulatory and Technical Requirements. Energy Procedia, 114, 5967-5980.

Harbert, W., Daley, T.M., Bromhal, G., Sullivan, C., Huang, L., 2016. Progress in monitoring strategies for risk reduction in geologic CO_2 storage. International Journal of Greenhouse Gas Control, 51, 260-275.

Hovorka, S.D., Meckel, T.A., Trevino, R.H., Lu, J., Nicot, J.-P., Choi, J.-W., Freeman, D., Cook, P., Daley, T.M., Ajo-Franklin, J.B., Freifeild, B.M., Doughty, C., Carrigan, C.R., La Brecque, D., Kharaka, Y.K., Thordsen, J.J., Phelps, T.J., Yang, C., Romanak, K.D., Zhang, T., Holt, R.M., Lindler, J.S., Butsch, R.J., 2011. Monitoring a large volume CO_2 injection: Year two results from SECARB project at Denbury's Cranfield, Mississippi, USA. Energy Procedia, 4, 3478-3485.

IEA, 2021. Net Zero by 2050, Paris, https://www.iea.org/reports/net-zero-by-2050.

IEAGHG, 2020. Monitoring and Modelling of CO_2 Storage: The Potential for Improving the Cost-Benefit Ratio of Reducing Risk, IEA/CON/19/255, IEA Greenhouse Gas R&D Programme.

Jacob, T., Bayer, R., Chery, J., Le Moigne, N., 2010. Time-lapse microgravity surveys reveal water storage heterogeneity of a karst aquifer. Journal of Geophysical Research: Solid Earth, 115, B06402.

Jacob, T., Rohmer, J., Manceau, J.C., 2016. Using surface and borehole time-lapse gravity to monitor CO_2 in saline aquifers: a numerical feasibility study. Greenhouse Gases: Science and Technology, 6, 34-54.

Jenkins, C., Chadwick, A., Hovorka, S.D., 2015. The state of the art in monitoring and verification—ten years on. International Journal of Greenhouse Gas Control, 40, 312–349.

Jenkins, C., 2020. The State of the Art in Monitoring and Verification: an update five years on. International Journal of Greenhouse Gas Control, 100, 103118, https://doi.org/10.1016/j.ijggc.2020.103118.

Kabirzadeh, H., Kim, J.W., Sideris, M.G., Vatankhah, S., 2020. Analysis of surface gravity and ground deformation responses of geological CO_2 reservoirs to variations in CO_2 mass and density and reservoir depth and size. Environmental Earth Sciences, 79, 163.

Kim, J., Xue, Z., Matsuoka, T., 2010. Experimental study on CO_2 monitoring and saturation with combined P-wave velocity and resistivity. International Oil and Gas Conference and Exhibition, SPE, Extended Abstracts, https://doi.org/10.2118/130284-MS.

Kragh, E., Christie, P., 2002. Seismic repeatability, normalized RMS, and predictability. The Leading Edge, 21, 640–647.

Krahenbuhl, R.A., Li, Y., 2012. Time-lapse gravity: A numerical demonstration using robust inversion and joint interpretation of 4D surface and borehole data. Geophysics, 77, G33-G43.

Krahenbuhl, R.A., Martinez, C., Li, Y., Flanagan, G., 2015. Time-lapse monitoring of CO_2 sequestration: A site investigation through integration of reservoir properties, seismic imaging, and borehole and surface gravity data. Geophysics, 80, WA15-WA24.

Lofts, J., Zett, A., Clifford, P., Li, Y., Krahenbuhl, R., Seshia, A., 2019. Three-Axis Borehole Gravity Logging for Reservoir Surveillance. SPE Middle East Oil and Gas Show and Conference. Manama, Bahrain, Society of Petroleum Engineers, 13.

Lumley, D., 2021, Long-Term Seismic Monitoring of CO_2 Sequestration Projects for 50-100 Years. AGU, New Orleans, December 12-17, 2021.

Mathieson, A., Midgely, J., Wright, I., Saoula, N., Ringrose, P., 2011. In Salah CO_2 Storage JIP: CO_2 sequestration monitoring and verification technologies applied at Krechba, Algeria. Energy Procedia, 4, 3596-3603.

NIST Mixture Property Database, NIST Standard Reference Database #14, 1992. U.S. Department of Commerce, National Institute of Standards and Technology (NIST).

Nooner, S.L., Eiken, O., Hermanrud, C., Sasagawa, G.S., Stenvold, T., Zumberge, M.A., 2007. Constraints on the in situ density of CO_2 within the Utsira formation from time-lapse seafloor gravity measurements. International Journal of Greenhouse Gas Control, 1, 198-214.

Park, J., Sauvin, G., Voge, M., 2017. 2.5D Inversion and Joint Interpretation of CSEM Data at Sleipner CO_2 Storage. Energy Procedia, 114, 3989-3996.

Pawar, R.J., Bromhal, G.S., Carey, J.W., Foxall, W., Korre, A., Ringrose, P.S., Tucker, O., Watson, M.N., White, J.A., 2015. Recent advances in risk assessment and risk management of geologic CO_2 storage. International Journal of Greenhouse Gas Control, 40, 292–311.

Popik, S., Pevzner, R., Tertyshnikov, K., Popik, D., Urosevic, M., Shulakova, V., Glubokovskikh, S., Gurevich, B., 2020. 4D surface seismic monitoring the evolution of a small CO_2 plume during and after injection: CO2CRC Otway Project study. Exploration Geophysics, doi: 10.1080/08123985.2020.1735934.

Pruess, K., 2004. The TOUGH codes–A family of simulation tools for multi-phase flow and transport processes in permeable media. Vadose Zone Journal, 3, 738–746.

Pruess, K., 2008. Leakage of CO_2 from geologic storage: Role of secondary accumulation at shallow depth. International Journal of Greenhouse Gas Control, 2, 37-46, ISSN 1750-5836, https://doi.org/10.1016/S1750-5836(07)00095-3.

Roach, L.A., White, D.J., Roberts, B., 2015. Assessment of 4D seismic repeatability and CO_2 detection limits using a sparse permanent land array at the Aquistore CO_2 storage site. Geophysics, 80, WA1-WA13.

Schmidt-Hattenberger, C., Bergmann, P., Labitzke, T., Wagner, F., Rippe, D., 2016. Permanent crosshole electrical resistivity tomography (ERT) as an established method for the long-term CO_2 monitoring at the Ketzin pilot site. International Journal of Greenhouse Gas Control, 52, 432-448.

Seyyedi, M., Mahmud, H.K.B., Verrall, M., Giwelli, A., Esteban, L., Ghasemiziarani, M., Clennell, B., 2020. Pore Structure Changes Occur During CO_2 Injection into Carbonate Reservoirs. Scientific Reports, 10, 3624.

Sherlock, D., Toomey, A., Hoversten, G.M., Gasperikova, E., Dodds, K., 2006. Gravity monitoring of CO_2 storage in a depleted gas field: A sensitivity study. Exploration Geophysics, 37, 37-43.

Telford, W.M., 1976. Applied Geophysics. Cambridge University Press, London.

Van Camp, M., de Viron, O., Pajot-Metivier, G., Casenave, F., Watlet, A., Dassargues, A., Vanclooster, M., 2016. Direct measurement of evapotranspiration from a forest using a superconducting gravimeter. Geophysical Research Letters, 43, 10225-10231.

Van Camp, M., de Viron, O., Watlet, A., Meurers, B., Francis, O., Caudron, C., 2017. Geophysics from Terrestrial Time-Variable Gravity Measurements. Reviews of Geophysics, 55, 938-992, http://dx.doi.org/10.1002/2017RG000566.

Vasco, D.W., Rucci, A., Ferretti, A., Novali, F., Bissell, R.C., Ringrose, P.S., Mathieson, A.S., Wright, I.W., 2010. Satellite-based measurements of surface deformation reveal fluid flow associated with the geological storage of carbon dioxide. Geophysical Research Letters, 37, L03303, doi:10.1029/2009GL041544.

Vermeul, V.R., Amonette, J.E., Strickland, C.E., Williams, M.D., Bonneville, A., 2016. An overview of the monitoring program design for the FutureGen 2.0 CO_2 storage site. International Journal of Greenhouse Gas Control, 51, 193-206.

Wang, Z., Harbert, W., Dilmore, R., Huang, L., 2018. Modeling of time-lapse seismic monitoring using CO_2 leakage simulations for a model CO_2 storage site with realistic geology: Application in assessment of early leak-detection capabilities. International Journal of Greenhouse Gas Control, 76, 39-52.

White, D., 2019. Integrated Geophysical Characterization and Monitoring at the Aquistore CO_2 Storage Site. In: Geophysics and Geosequestration, Davis, T.L., Landro, M., and Wilson, M. (Eds.), Cambridge University Press, pp. 257-279.

Wilkinson, M., Mouli-Castillo, J., Morgan, P., Eid, R., 2017. Time-lapse gravity surveying as a monitoring tool for CO_2 storage. International Journal of Greenhouse Gas Control, 60(Supplement C), 93-99.

Yang, X., Lassen, R.N., Jensen, K.H., Looms, M.C., 2015. Monitoring CO_2 migration in a shallow sand aquifer using 3D crosshole electrical resistivity tomography, International Journal of Greenhouse Gas Control, 42, 534-544.

Yang, X., Buscheck, T.A., Mansoor, K., Wang, Z., Carroll, S.A., 2018a. Effectiveness of Geophysical Monitoring Methods in Detecting Brine and CO_2 Leakage in Underground Sources of Drinking Water. LLNL-TR-752304; Lawrence Livermore National Laboratory, Livermore, CA.

Yang, X., Buscheck, T.A., Mansoor, K., Carroll, S.A., 2019. Assessment of Geophysical Monitoring Methods for Detection of Brine and CO_2 Leakage in Drinking Aquifers. International Journal of Greenhouse Gas Control, 90, 102803, https://doi.org/10.1016/j.ijggc.2019.102803.

Yang, Ya-Mei, Dilmore, R.M., Bromhal, G.S., Small, M.J., 2018b. Toward an adaptive monitoring design for leakage risk – Closing the loop of monitoring and modeling. International Journal of Greenhouse Gas Control, 76, 125–141.

Yilmaz, O., 2001. Seismic data analysis, Investigations in Geophysics, Vol. 1, p. 1809. Society of Exploration Geophysicists. Tulsa.

Zhang, K., Wu, Y.S., Pruess, K., 2008. User's Guide for TOUGH2-MP - a Massively Parallel Version of the TOUGH2 Code. Lawrence Berkeley National Laboratory, Berkeley, CA, USA.

Zhang, R., R. Ghosh, M. K. Sen, S. Srinivasan, 2013. Time-lapse surface seismic inversion with thin bed resolution for monitoring CO_2 sequestration: A case study from Cranfield, Mississippi. International Journal of Greenhouse Gas Control, 18, 430-438.

ACRONYMS

2D	Two-dimensional
3D	Three-dimensional
4D	Four-dimensional, time being the fourth dimension
CSEM	Controlled Source ElectroMagnetics
CMP	Common Mid-Point
CO_2	Carbon Dioxide
EM	ElectroMagnetic
ERT	Electrical Resistance Tomography
GCS	Geologic Carbon Storage/Sequestration
LSRTM	Least-Squares Reverse-Time Migration
MT	Magnetotellurics
nRMS	Normalized Root Mean Square
SNR	Signal-to-Noise Ratio
TDS	Total Dissolved Solids

FIGURE CAPTIONS

Figure 1. Monitoring at a GCS site and objectives of this study.

Figure 2. Size of 1,000 tonne accumulations as a function of depth below the surface for CO_2 saturation of (a) 5%, (b) 10%, and (c) 20%. The radii of the CO_2 plume in 10-, 30-, and 100-m-thick layers are shown in blue, magenta, and red, respectively.

Figure 3. Differences between migrated sections for the initial conditions and 1,000 tonne CO_2 accumulations at depths of (a) 500 m, (b) 800 m, (c) 1000 m, and (d) 1300 m. A saturation of 20% and 30-m thickness of the cone-shaped accumulation is used for these calculations. The seismic response for the accumulation at depths of 500 and 800 m is detectable; however, the response of the accumulation at depths of 1000 and 1300 m is in the noise level of the survey.

Figure 4. CO_2 saturation cross-sections for a scenario with (a) a single secondary CO_2 plume in Olcese Formation and (b) three secondary CO_2 plumes present in the (1) Olcese, (2) Santa Margarita, and (3) Etchegoin formations. The secondary CO_2 plume in Olcese Formation is within the storage complex.

Figure 5. (a) Actual model P-wave velocity difference for a CO_2 plume at 1500 m depth, and normalized P-wave velocity image difference using (b) noise-free data, (c) noisy data with

SNR=5, and (d) noisy data with SNR=2. The estimated location of the secondary plume in (b) and (c) agrees very well with the actual model (a); with significant noise in the data (d), the detection capabilities degrade.

Figure 6. Image SNR versus $\sqrt{N}$ for acquisition geometry with sparser receivers/shots (red dots) and shorter recording offsets (blue dots). The dashed black curve is for image SNR to $\sqrt{N}$ = C, where C is a constant factor.

Figure 7. (a) Pore fluid resistivity as a function of TDS and temperature shown in color; (b) rock bulk resistivity (ρ_b) as a function of CO_2 saturation and porosity (ϕ) (shown in color). Pore fluid resistivity is 0.33 Ohm-m, a =1, m = 2, and n=2. Pore fluid resistivity decreases with increasing TDS or temperature. Rock bulk resistivity increases with CO_2 saturation and decreases with porosity.

Figure 8. Apparent resistivity changes as a function of target depth for surface resistivity techniques. The response due to CO_2 presence decreases with an increasing target depth.

Figure 9. (a) A model with CO_2 plumes at three different depths: (1) 1500 m, (2) 1000 m, and (3) 300 m; receivers are shown as black circles, and transmitters are shown as black rectangles. The difference in electric field amplitude for (b) surface array and (c) borehole-to-surface array due to CO_2 plumes shown in (a) and (b).

Figure 10. (a) The model with CO_2 plume at 1500-m depth: receivers are shown as red circles, the transmitter is shown as a red rectangle; (b) changes in subsurface resistivity due to CO_2 presence at t1+40 years; and (c) difference in electric field amplitude at t_1, t_1+5, t_1+10, t_1+15, and t_1+40 years using borehole-to-surface EM configuration (t_1 is the time of the seismic survey shown in Figure 5).

Figure 11. CO_2 plume size (cylinder radius) as a function of CO_2 saturation and depth to produce a signal of (a) -4 μGal and (b) -10 μGal. The radii of 250, 500, 1000, 2000, and 3000 m are shown as solid, dashed, dot-dashed, double dot-dashed, and dotted lines, respectively. The deeper the plume, the larger the size or CO_2 saturation required to produce the same signal measured on the surface.

Figure 12. CO_2 plume size (cylinder radius) as a function of CO_2 mass and depth to produce a signal of (a) -4 μGal and (b) -10 μGal. The radii of 250, 500, 1000, 2000, and 3000 m are shown as solid, dashed, dot-dashed, double dot-dashed, and dotted lines, respectively. The CO_2 mass increases with plume size and depth. The curves asymptote and make it difficult to determine the correct CO_2 mass at great depths.

Figure 13. CO_2 plume radius as functions of depth for a variable CO_2 saturation (shown in color) for signal levels of (a) -4 μGal and (b) -10 μGal. The higher the saturation and the larger the plume size, the greater the depth of detection.

Figure 14. Evolution of the gravity response for a CO_2 accumulation occurring at a depth of 1500 m, with increasing radius and variable CO_2 saturation. Two dashed red lines represent the detection thresholds of -4 μGal and -10 μGal. Black diamonds at t_1, t_1+5, t_1+10, t_1+15, and t_1+40 years correspond to the simplified two-cylinder model used to approximate the secondary plumes shown in Figure 10a (t_1 is the time of the seismic survey shown in Figure 5).

Figure 15. A conceptual model for borehole gravity calculations. The 3D prism with Δd density contrast represents the CO_2 plume, for which depth and horizontal dimensions can vary; plus symbols indicate measurement locations.

Figure 16. Maximum distance of detection vs. depth of a 5-μGal change in the vertical gravity component g_z for (a) 10,000 tonnes and (b) 100,000 tonnes CO_2 mass and bulk density changes varying from 1% to 5 % are shown in color.

Figure 17. Maximum distance of detection vs. depth of a 10-μGal change in the vertical gravity component g_z for (a) 10,000 tonnes and (b) 100,000 tonnes CO_2 mass and bulk density changes varying from 1% to 5 % are shown in color.

LIST OF TABLES